poloidal field component B^P, naturally provides stable hoop stresses that are the only known collimation mechanism for the large-scale jet morphology of quasars (*21*, *22*). The nonrelativistic outer layer observed in some jets can be supported by a coexisting, enveloping, relatively low-power wind or jet from the accretion disk (*23*).

The jets composed of a bundle of strings like those in the simulation are energetic enough to power quasar jets. The Poynting flux transported by a pair of bipolar collimated jets is approximately (*2*)

$$S \approx \frac{[\Omega_F \Phi]^2}{2\pi^2 c} \quad (2)$$

The total magnetic flux in the jet is Φ. The field line angular velocity Ω_F varies from near zero at the outer boundary of the ergosphere to the horizon angular velocity $\Omega_H \approx 10^{-4}$ s^{-1} in the inner ergosphere. Thus, $S \sim (\Omega_H \Phi)^2 = (a\Phi/2Mr_+)^2 \sim (a\Phi/M)^2$ for rapidly rotating black holes. Consequently, there are three important parameters that determine jet power: M, a, and B. For rapidly spinning black holes, the surface area of the equatorial plane in the ergosphere becomes quite large; for $a/M = 0.996$, it is $\approx 30\ M^2$ (*2*). Various accretion flow models yield a range of achievable ergospheric field strengths $B \sim 10^3$ G to 2×10^4 G that equate to $\Phi \sim 10^{33}$ G-cm^2 to 10^{34} G-cm^2 (*2*, *14*, *24*). Inserting these results into Eq. 2 yields a jet luminosity of $\approx 10^{45}$ to 5×10^{47} ergs/s. This is consistent with the estimates of the kinetic luminosity of powerful quasar jets (*1*). The maximum value of the flux noted above occurs when the persistent accretion of magnetic flux has a pressure that is capable of pushing the inner edge of the accretion disk out of the ergosphere (known as magnetically arrested accretion) (*15*, *16*). This maximum flux inserted in Eq. 2 equates to a jet power that is $\approx$ 5 to 25 times the bolometric thermal luminosity of the accretion flow in the disk models considered in (*2*, *24*).

If 10% of the central black holes in quasars were magnetized by the accretion of vertical flux, this would explain the radio loud/radio quiet quasar dichotomy. To elevate this above a conjecture requires observational corroboration of the putative magnetosphere in radio loud quasars. A significant flux trapped between the black hole and the accretion disk should modify the innermost regions of the accretion flow. Thus, one can look for a distinction between radio loud and radio quiet quasar thermal emission at the highest frequencies. There might already be evidence to support this. The accretion flow radiation has a high-frequency tail in the EUV (extreme ultraviolet). Hubble Space Telescope (HST) data indicate that radio quiet quasars have an EUV excess as compared to radio loud quasars (*25*). The EUV suppression has been explained by the interaction of the magnetic field with the inner edge of the disk, displacing the EUV-emitting gas in radio loud quasars (*26*).

The simulations presented here explain five important observations of radio loud quasars: the production of a collimated jet (based on radio observations); a power source (the black hole) that is decoupled from the accretion flow properties to first order [broadband radio-to-ultraviolet observations indicate that a quasar can emit most of its energy in a jet without disrupting the radiative signatures of the accretion flow (see the SOM)]; the suppression of the EUV in radio loud quasars (from HST observations); the relativistic velocity of the jet (from VLBI data); and the maximal kinetic luminosity of the quasar jets (from broadband radio and x-ray observations of radio lobes). The GHM process might also drive jets in other systems such as microquasars or gamma-ray bursts (*27*, *28*). However, microquasars show correlations between accretion disk emission and jet properties, unlike quasars (*29*). Consequently, there is no strong observational reason to prefer the black hole over the accretion disk as the primary power source for microquasars, as there is with quasar jets.

References

1. K. Blundell, S. Rawlings, *Astron. J.* **119**, 1111 (2000).
2. B. Punsly, *Black Hole Gravitohydromagnetics* (Springer-Verlag, New York, 2001).
3. M. J. Rees, E. S. Phinney, M. C. Begelman, R. D. Blandford, *Nature* **295**, 17 (1982).
4. M. C. Begelman, R. D. Blandford, M. J. Rees, *Rev. Mod. Phys.* **56**, 255 (1984).
5. S. Koide, K. Shibata, T. Kudoh, D. L. Meier, *Science* **295**, 1688 (2002).
6. S. Koide, *Phys. Rev. D* **67**, 104010 (2003).
7. S. Koide, *Astrophys. J. Lett.* **606**, L45 (2004).
8. S. Komissarov, *Mon. Not. R. Astron. Soc.* **350**, 1431 (2004).
9. S. Hirose, J. Krolik, J. De Villiers, *Astrophys. J.* **606**, 1083 (2004).
10. J. McKinney, C. Gammie, *Astrophys. J.*, in press; preprint available at http://arxiv.org/abs/astro-ph/0404512.
11. M. Christensson, M. Hindmarsh, *Phys. Rev.* **D60**, 063001-1 (1999).
12. V. S. Semenov, S. A. Dyadechkin, I. B. Ivanov, H. K. Biernat, *Phys. Scripta* **65**, 13 (2002).
13. T. J. Jones, *Astron. J.* **120**, 2920-2927 (2000).
14. D. Macdonald, K. Thorne, R. Price, X.-H. Zhang, in *Black Holes The Membrane Paradigm*, K. Thorne, R. Price, D. Macdonald, Eds. (Yale Univ. Press, New Haven, CT, 1986), pp. 121–145.
15. I. V. Igumenshchev, R. Narayan, M. A. Abramowicz, *Astrophys. J.* **592**, 1042 (2003).
16. R. Narayan, I. V. Igumenshchev, M. A. Abramowicz, *Publ. Astron. Soc. Jpn.* **55**, 69 (2003).
17. J. Bardeen, *Nature* **226**, 64 (1970).
18. K. Kellerman *et al. Astrophys. J.* **609**, 539 (2004).
19. R. V. E. Lovelace, M. M. Romanova, *Astrophys. J. Lett.* **596**, 159 (2003).
20. V. Nektarios, A. Konigl, *Astrophys. J.* **605**, 656 (2004).
21. G. Benford, *Mon. Not. R. Astron. Soc.* **183**, 29 (1978).
22. P. Hardee, in *Cygnus A–Study of a Radio Galaxy*, C. L. Carilli, D. E. Harris, Eds. (Cambridge Univ. Press, New York, 1996), pp. 113–120.
23. G. Henri, G. Pelletier, *Astrophys. J.* **383**, L7 (1991).
24. F. Casse, R. Keppens, *Astrophys. J.* **601**, 90 (2004).
25. W. Zheng, G. A. Kriss, R. C. Telfer, J. P. Grimes, A. F. Davidsen, *Astrophys. J.* **475**, 469 (1997).
26. B. Punsly, *Astrophys. J.* **527**, 609 (1999).
27. S. Eikenberry *et al.*, *Astrophys. J.* **494**, L61 (1998).
28. J. Katz, *Astrophys. J.* **490**, 633 (1997).
29. R. Fender, in *Compact Stellar X-Ray Sources*, W. H. G. Lewin, M. van der Klis, Eds. (Cambridge Univ. Press, Cambridge, in press) (preprint available at http://arxiv.org/abs/astro-ph/0303339).

Supporting Online Material

www.sciencemag.org/cgi/content/full/305/5686/978/DC1
Methods
SOM Text
Figs. S1 and S2
References
Movies S1 to S5

24 May 2004; accepted 8 July 2004

Localization of Fractionally Charged Quasi-Particles

Jens Martin,[1]* Shahal Ilani,[1]† Basile Verdene,[1] Jurgen Smet,[2] Vladimir Umansky,[1] Diana Mahalu,[1] Dieter Schuh,[3] Gerhard Abstreiter,[3] Amir Yacoby[1]

An outstanding question pertaining to the microscopic properties of the fractional quantum Hall effect is understanding the nature of the particles that participate in the localization but that do not contribute to electronic transport. By using a scanning single electron transistor, we imaged the individual localized states in the fractional quantum Hall regime and determined the charge of the localizing particles. Highlighting the symmetry between filling factors 1/3 and 2/3, our measurements show that quasi-particles with fractional charge $e^* = e/3$ localize in space to submicrometer dimensions, where e is the electron charge.

The quantum Hall effect (QHE) arises when electrons confined to two dimensions are subject to a strong perpendicular magnetic field. The magnetic field quantizes the kinetic energy and leads to the formation of Landau levels (LL). Energy gaps appear in the spectrum whenever an integer number of LLs is filled. Disorder broadens the LLs and gives rise to bands of extended states surrounded by bands of localized states. Localization plays a fundamental role in the universality and robustness of quantum Hall phenomena. In the localized regime, as the den-

sity of electrons increases, only localized states are being populated and hence the transport coefficients remain universally quantized (*1*). Conversely, when the Fermi energy lies within the bands of extended states, the transport coefficients vary indicating transitions between quantum Hall phases (*2*, *3*).

When the filling of the lowest LL is less than one, the fractional quantum Hall effect (FQHE) emerges (*4*) as a result of Coulomb interactions between electrons. The Coulomb interactions give rise to a new set of energy gaps occurring at fractional fillings $\nu = \frac{q}{2q \pm 1}$ with q being an integer. Soon after the discovery of the FQHE, a theory was presented for the ground state properties of these unique phases (*5*), in which the low energy excitations above these ground states are fractionally charged with $e^* = \frac{e}{2q \pm 1}$. Only recently, through use of resonant tunneling and shot noise measurements, were such fractionally charged quasi-particles shown to exist experimentally (*6*–*10*). These measurements convincingly demonstrate that the fractionally charged quasi-particles participate in transport and are hence extended along the edge of the sample. However, what is the nature of the particles that participate in the localization and do not contribute to transport? We address this question with the use of a scanning single electron transistor (SET), which enables us to detect directly the position and charge of the localizing particles across the various integer and fractional quantum Hall phases.

Our experimental method is described in detail elsewhere (*11*, *12*). A SET is used to measure the local electrostatic potential of a two-dimensional electron gas (2DEG) (*13*). At equilibrium, changes in the local electrostatic potential result from changes in the local chemical potential, which can be induced, for example, by varying the average electron density (*14*) with the use of a back gate. The local derivative of the chemical potential, μ, with respect to the electronic density, $d\mu/dn$, is inversely proportional to the local compressibility and depends strongly on the nature of the underlying electronic states (*15*, *16*). In the case of extended electrons, charge is spread over large areas; hence, the chemical potential will follow continuously the variations in density, and the measured inverse compressibility will be small and smooth. However, in the case of localized electrons the local charge density can increase only in steps of e/ξ^2, where ξ is the localization length. Hence, the system becomes compressible only when a localized state is being populated, producing a jump in the local chemical potential and a spike in its derivative, the inverse compressibility. Thus, by using the scanning SET in the localized regime, we were able to image the position and the average density at which each localized state is populated. Three different GaAs-based 2DEGs with peak mobilities of 2×10^6 cm^2/ V^{-1} s^{-1} (V6-94 and V6-131) and 8×10^6 cm^2/ V^{-1} s^{-1} (S11-27-01.1) were studied.

We start by reviewing the properties of localized states in the integer QHE. Figure 1A shows a typical scan of $d\mu/dn$ as function of the average electron density, n, and position, x, near the integer quantum Hall phase $\nu = 1$. Each black arc corresponds to the charging line of an individual localized state. At any particular location, as the density is varied through $\nu = 1$, electrons occupying localized states give rise to negative spikes. The tip detects only charging of localized states situated directly underneath it. The measured spatial extent of each localized state (black arc) is therefore determined by the size of the localized state convoluted with the spatial resolution of the tip. A small tip bias is responsible for the arcing shape of each charging line. Figure 1A shows that electrons do not localize randomly in space but rather pile up at particular locations. Moreover, the spacing within each charging spectrum is regular. Such charging spectra are reminiscent of Coulomb blockade physics, where charge quantization governs the addition spectrum of a quantum dot. In the microscopic description of localization in the integer QHE (*17*), the formation of dots was explained with use of a simple model that incorporates Coulomb interaction between electrons and thereby accounts for changes in the screening properties of the 2DEG as the filling factor is varied (*18*–*21*). For completeness, we briefly sketch the model for $\nu = 1$ because it will prove to be essential for understanding the measured spectra at fractional filling factors.

An intuitive picture of localization driven by Coulomb interaction is obtained by tracing the self-consistent density distribution as a function of B and n. Far from integer filling, the large compressibility within an LL provides nearly perfect screening of the disorder potential. This is accomplished by creating a nonuniform density profile with a typical length scale larger than the magnetic length, $l_m = \sqrt{h/(eB)}$ (Fig. 1B). The corresponding potential distribution in the plane of the 2DEG is equal and opposite in sign to the disorder potential. Because of a large energy gap between the LLs, the density, n_{LL}, cannot exceed one electron per flux quanta, $n_{max} = B/\phi_0$, and is therefore constrained by $0 \leq n_{LL} \leq n_{max}$. At the center of the LL (far from integer filling), this constraint is irrelevant because the variations in density required for screening are smaller than n_{max}, thus leading to nearly perfect screening (Fig. 1B). Each electron added to the system experiences this flat potential and thus, within this approximation, is completely delocalized. With increasing filling factor, the density distribution increases uniformly, maintaining its spatial structure. However, near $\nu = 1$ the average density approaches n_{max} and the required density distribution for perfect screening exceeds n_{max} at certain locations. Because of a large energy gap between the LLs, n_{LL} cannot exceed n_{max}, and the density at these locations becomes pinned to n_{max}. Local incompressible regions are formed in which the bare disorder potential is no longer screened, coexisting with compressible regions where the LL is still only partially full [$0 < n_{LL}(x) < n_{max}$, where

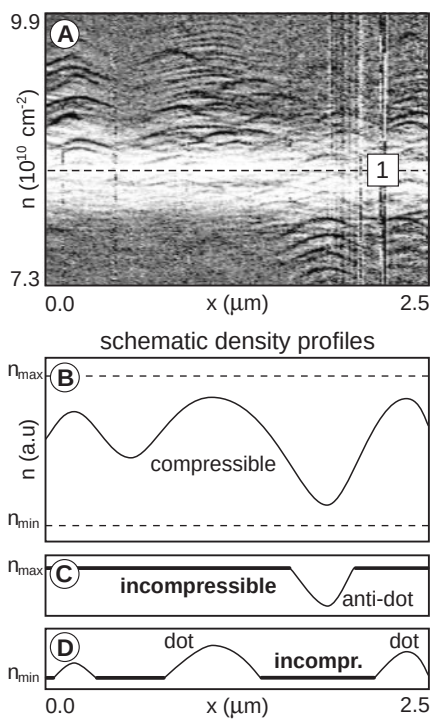

Fig. 1. (**A**) Density-position scan of $d\mu/dn$ near $\nu = 1$ [$B = 3.5$ T, temperature (T) = 300 mK, sample V6-94]. Each black line corresponds to a localized state. The central white area corresponds to the incompressible region near complete filling of the first LL (the dashed line marks $\nu = 1$). Localized states group into families, which appear as QD spectra above (and antidot spectra below) the incompressible region. (**B**) Far from integer filling, the large compressibility within an LL provides nearly perfect screening at the cost of a nonuniform density profile. Here, a schematic density profile is shown. n_{max} and n_{min} indicate the maximum and minimal densities, respectively, within an LL. a.u., arbitrary units. (**C**) In case the average density is slightly less than complete filling, the 2DEG becomes incompressible whenever the maximum allowed density n_{max} is reached and remains compressible only in a small area. This area forms an antidot whose energy levels are determined by the charging energy. (**D**) Once the average density is slightly higher than complete filling, compressible areas appear in the next LL and form QDs.

[1]Weizmann Institute of Science, Condensed Matter Physics, 76100 Rehovot, Israel. [2]Max-Planck Institut für Festkörperforschung, D-70569 Stuttgart, Germany. [3]Walter-Schottky Institut, Technische Universität München, D-85748 Garching, Germany.

*To whom correspondence should be addressed. E-mail: jens.martin@weizmann.ac.il

†Present address: Laboratory of Atomic and Solid State Physics, Cornell University, Ithaca, New York 14853, USA.

x is the position] and the local potential is screened (Fig. 1C). Once an incompressible region surrounds a compressible region, it behaves as an antidot whose charging is governed by Coulomb blockade physics. Antidots are therefore formed in the regions of lowest local density, and as the filling increases further the antidot will be completely emptied. Spatially separated from such local density minima are the maxima of the density profile, where the filling of the next LL will first occur, now as quantum dots (QDs) (Fig. 1D).

An important consequence of the above model is that the spectra of localized states are defined only by the bare disorder potential, the presence of an energy gap, causing an incompressible quantum Hall liquid surrounding the QD, and the charge of the localizing particles. It is the character of the boundary that determines the addition spectra of the quantum dot, and it is because of Coulomb blockade that the charge directly determines the number of charging lines and their separation and their strength. Therefore, the number of localized states does not depend on the magnetic field. A different magnetic field will simply shift n_{max} and hence the average density at which localization commences. Therefore, the local charging spectra will evolve as a function of density and magnetic field exactly parallel to the quantized slope of the quantum Hall phases, $dn/dB = \nu e/h$ (Fig. 2, A, I and III).

The presence of an energy gap at fractional filling factors implies that the model for localization described above may also apply to the fractional quantum Hall regime. As in the integer case, the local charging spectra contain a fixed number of localized states (independent of B) that evolve in density and magnetic field according to $dn/dB = \nu e/h$. The difference between the integer and fractional case is that now the slopes are quantized to fractional values (Fig. 2, A, II and IV, and B). The invariance of the local charging spectra along fractional filling factors can also be inferred from Fig. 2, C and D, where we show that the spatially dependent charging spectra at $\nu = 1/3$ for two different magnetic fields are identical. Our observations confirm that the microscopic mechanism for localization in the fractional quantum Hall regime is identical to that of the integer case; i.e., localization is driven by Coulomb interaction. The QDs that appear near integer or fractional filling factors are, therefore, identical. Their position, shape, and size are solely determined by the underlying bare disorder potential. This conclusion allows us to determine the charge of localizing particles in the fractional quantum Hall regime by comparing the charging spectra of integer and fractional filling factors. Charging spectra corresponding to the localization of electrons should look identical to those seen at integer filling. On the other hand, the charging spectra of fractionally charged quasi-particles, with $e^* = e/3$ for example, would have a denser spectrum with three times more charging lines, i.e, localized quasi-particle states. We emphasize that the slope of the localized states in the n-B plane merely indicates the filling factor they belong to rather than their charge.

The spatially resolved charging spectra for integer $\nu = 1$ and $\nu = 3$ and fractional $\nu = 1/3$ and $\nu = 2/3$ are shown in Fig. 3. All the scans are taken along the same line in space and cover the same density interval. The scans differ only in the starting density and the applied magnetic field. The spatially resolved charging spectra for integer fillings in Fig. 3, A and B, look identical. As expected, despite the different filling factors the measured spectra of localized states appear at the same position in space and with identical spacing. Figure 3, C and D, shows spatially resolved charging spectra at $\nu = 1/3$ and $\nu = 2/3$. Here also, the two spectra look identical. Moreover, the charging spectra are seen at the same locations as in the integer case. The only difference between the spectra taken at integer and fractional filling is the number of charging lines within a given range of densities. At $\nu = 1/3$ and $\nu = 2/3$, there are three times more charging lines and the separation between charging lines is three times smaller. This can be also seen in Fig. 3, E to H.

Our model assumes large energy gaps relative to the bare disorder potential. In practice, however, the gap for fractional filling factors is considerably smaller than in the integer case. In order to have a comparable gap in the integer and fractional regime, we first measured the integer quantum Hall phases at low magnetic field and then measured the fractions at high field. Such a comparison is meaningful because the number of localized states is independent of magnetic field. In order to eliminate any doubt that the higher number of localized states in the fractional regime result from the measurement at higher fields, we also compare in Fig. 3, G and H, spectra of $\nu = 1$ and $\nu = 1/3$ measured at the same magnetic field, $B = 7.25$ T. Regardless of field or density, the spectrum of $\nu = 1/3$ is three times denser than that of $\nu = 1$.

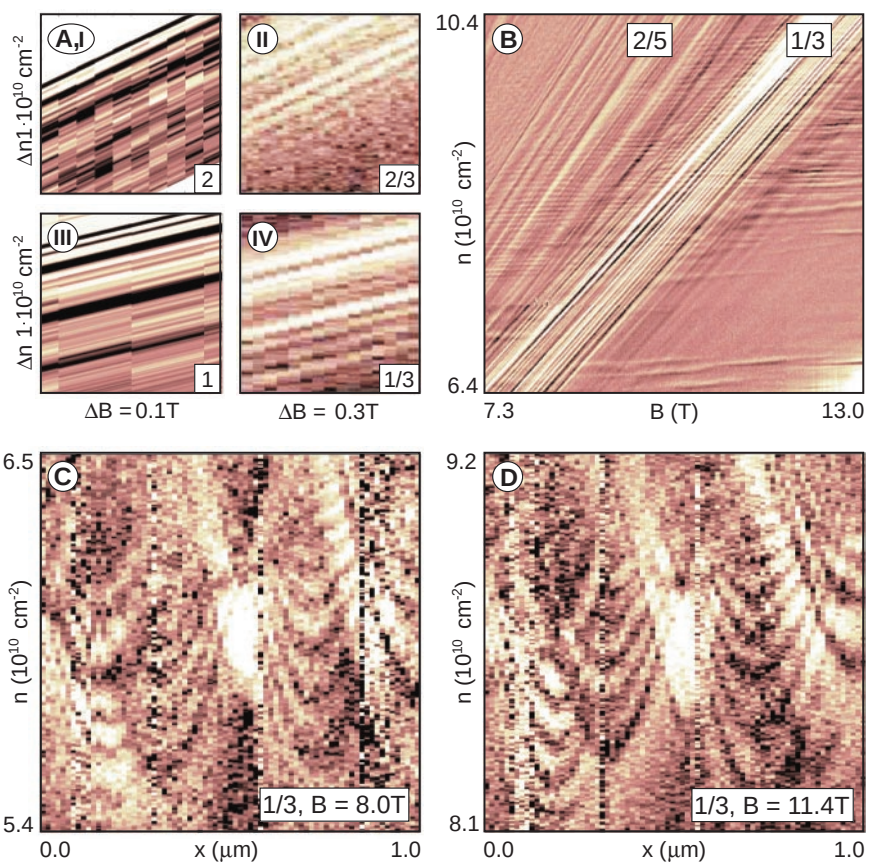

Fig. 2. (**A**) Density-magnetic field scans for integer $\nu = 2$ (I) and $\nu = 1$ (III) and for fractional $\nu = 2/3$ (II) and $\nu = 1/3$ (IV) (sample V6-131). All scans cover the same density range Δn. The range in magnetic field is three times larger for the fractional fillings. Each black line corresponds to a localized state. (**B**) This density-magnetic field scan covers a much larger range in field and density than (A) and shows localized states for $\nu = 1/3$ and $\nu = 2/5$ (sample S11-27-01.1, $T < 100$ mK). Even for a change of the magnetic field by a factor of 2, the number of localized states does not change. (**C**) Density-position scan for $\nu = 1/3$ at $B = 8$ T (sample V6-131, $T = 300$ mK). Just as for the integer QHE, the localized states appear as QD spectra. (**D**) Scan at the same position as in (C) but at $B = 11.4$ T. The same QD spectra are recovered at higher density. They are better resolved as a result of the enhanced gap size at higher fields.

Our results constitute direct evidence that quasi-particles with charge $e/3$ localize at $\nu = 1/3$ and $\nu = 2/3$. Moreover, our results highlight the symmetry between filling factors 1/3 and 2/3, indicating directly that at $\nu = 2/3$ the quasi-particle charge is $e/3$. In contrast to the experiments on resonant tunneling across an artificial antidot (*6*, *7*), our measurements probe generic localized states in the bulk of the 2DEG. The localization area, ξ^2, can be inferred from the charging spectra by using the condition for charge neutrality: $e^* = e\Delta n\xi^2$, where is the measured spacing between charging lines in units of density. For the left spectrum in Fig. 1D, $e^* = e/3$ and $\Delta n \approx 1 \times 10^{11}$ cm^{-2}, which corresponds to $\xi \approx 200$ nm, indicating quasi-particle localization to submicrometer dimensions. The extracted localization length provides further support for the validity of our model, which assumes long-range disorder relative to the magnetic length.

So far we have concentrated on the level spacing of the charging spectra. We now turn to address the amplitude of a single charging event. The integrated signal across a single charging event (spike) is the change in the local chemical potential associated with the addition of a single charge quantum, given by $\Delta\mu = e^*/C_{tot}$, where C_{tot} is the total capacitance of the QD. Because the capacitance between the QD and its surrounding is unknown experimentally, one cannot use this jump in chemical potential to determine the absolute charge of the localized particle. However, knowing that the QDs formed at integer and fractional filling are identical, one expects C_{tot} to be unchanged. Therefore, the ratio of $\Delta\mu$ at different filling factors is a measure of the ration of quasi-particle charge. Figure 4 shows a cross section of the measured $d\mu/dn$ through the center of a QD and the integrated signal $\Delta\mu$. One can clearly see that the step height in the fractional regime is only about 1/3 of the step height in the integer regime, confirming the localization of quasi-particles with $e^* = e/3$ for both $\nu = 1/3$ and $\nu = 2/3$.

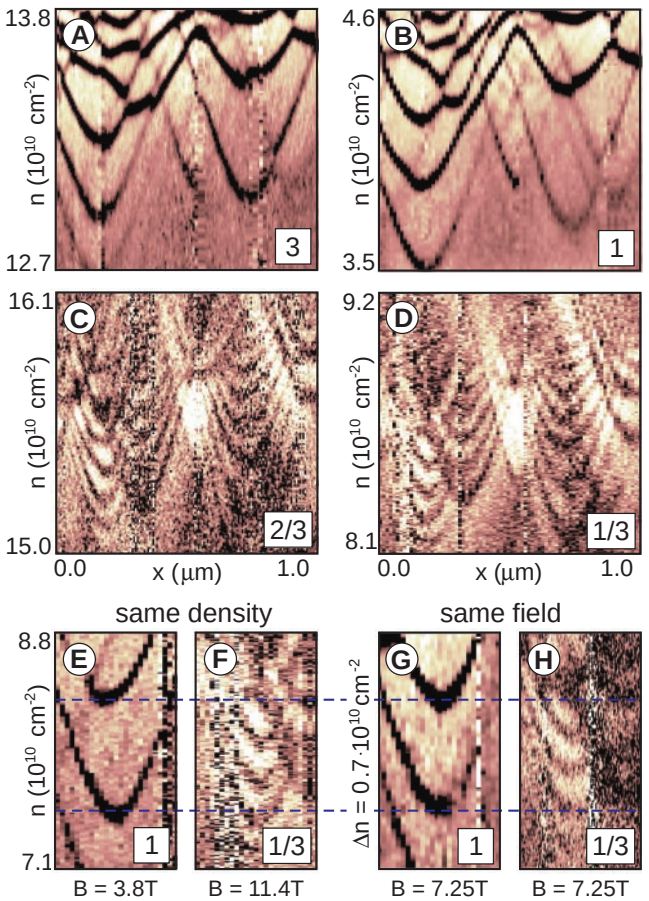

Fig. 3. (**A**) Density-position scan for $\nu = 3$ ($B = 1.9$ T, $T = 300$ mK, sample V6-131). The level spacing decreases slightly with increasing density, indicating the spectra of QDs. (**B**) Density-position scan at the same position as (A) for $\nu = 1$ ($B = 1.9$ T). (**C**) Density-position scan for $\nu = 2/3$ ($B = 10$ T) at the same position as the integer scans. (**D**) Density-position scan for $\nu = 1/3$ ($B = 11.4$ T, same as in Fig. 2D). Comparison between integer and fractional filling factors reveals three times denser LS spectra for the fractional regime. (**E**) Left dot at $\nu = 1$ measured at the same density (one-third the magnetic field) as scan for $\nu = 1/3$ in (**F**). (**G**) Left dot at $\nu = 1$ measured at the same magnetic field (3 times the density) as the scan for $\nu = 1/3$ in (**H**). The dashed lines serve as a guide to the eye to emphasize the difference in the level spacing between $\nu = 1$ and $\nu = 1/3$. The level spacing is independent of magnetic field and density.

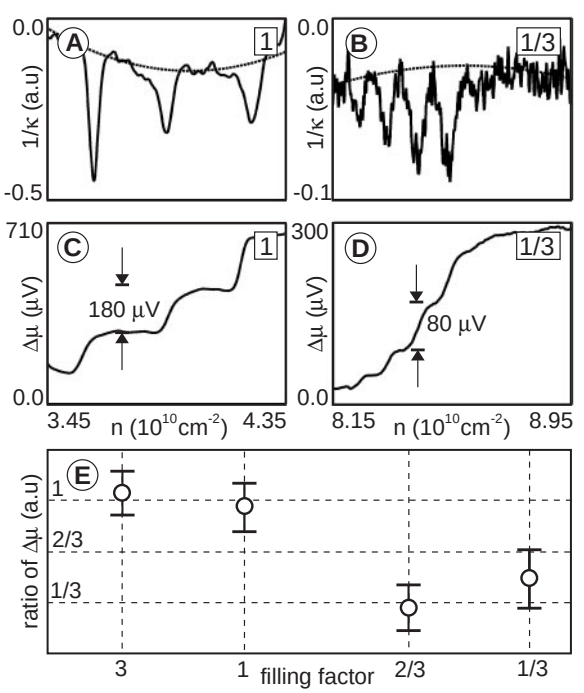

Fig. 4. (**A**) Cross section of the measured compressibility, κ, through the center of the left dot for $\nu = 1$ (Fig. 3B). For integration, the background compressibility (dotted line) is subtracted. (**B**) Cross section through the center of the left dot for $\nu = 1/3$ (Fig. 3D). (**C**) Integrated signal (chemical potential μ) with background correction for $\nu = 1$. Each step corresponds to one electron or quasi-particle entering the QD. (**D**) Integrated signal with background correction for $\nu = 1/3$. (**E**) Step height for the left dot for the various integer and fractional filling factors.

References and Notes

1. R. E. Prange, S. M. Girvin, Eds., *The Quantum Hall Effect* (Springer-Verlag, New York, ed. 2, 1990), chap. 1.
2. S. Kivelson, D. H. Lee, S. C. Zhang, *Phys. Rev. B* **46**, 2223 (1992).
3. B. Huckestein, *Rev. Mod. Phys.* **67**, 357 (1995).
4. D. C. Tsui, H. L. Stormer, A. C. Godard, *Phys. Rev. Lett.* **48**, 1559 (1982).
5. R. B. Laughlin, *Phys. Rev. Lett.* **50**, 1359 (1983).
6. V. J. Goldman, B. Su, *Science* **267**, 1010 (1995).
7. J. D. F. Franklin *et al.*, *Surf. Sci.* **361-362**, 17 (1996).
8. L. Saminadayar, R. V. Glattli, Y. Jin, B. Etienne, *Phys. Rev. Lett.* **79**, 2526 (1997).
9. M. Reznikov, R. de Picciotto, T. G. Griffiths, M. Heiblum, V. Umansky, *Nature* **399**, 238 (1999).
10. R. de Picciotto *et al.*, *Nature* **389**, 162 (1997).
11. M. J. Yoo *et al.*, *Science* **276**, 579 (1997).
12. A. Yacoby, H. F. Hess, T. A. Fulton, L. N. Pfeiffer, K. W. West, *Solid State Commun.* **111**, 1 (1999).
13. N. B. Zhitenev *et al.*, *Nature* **404**, 473 (2000).
14. J. P. Eisenstein, L. N. Pfeiffer, K. W. West, *Phys. Rev. B* **50**, 1760 (1994).
15. S. Ilani, A. Yacoby, D. Mahalu, H. Shtrikman, *Phys. Rev. Lett.* **84**, 3133 (2000).
16. S. Ilani, A. Yacoby, D. Mahalu, H. Shtrikman, *Science* **292**, 1354 (2001).
17. S. Ilani *et al.*, *Nature* **427**, 328 (2004).
18. A. L. Efros, A. F. Ioffe, *Solid State Commun.* **67**, 1019 (1988).
19. D. B. Chklovskii, P. A. Lee, *Phys. Rev. B* **48**, 18060 (1993).
20. N. R. Cooper, J. T. Chalker, *Phys. Rev. B* **48**, 4530 (1993).
21. I. Ruzin, N. Cooper, B. Halperin, *Phys. Rev. B* **53**, 1558 (1996).

22. This work is supported by the Israel Science Foundation, the Minerva Foundation, and the Fritz Thyssen Stiftung.

5 May 2004; accepted 9 July 2004